Supplementary information:

Section S1: Computational Details

DFT-based first-principles calculations for vacancy formation energy for all the systems i.e., ferrite and other spinel ferrite systems (MFe_2O_4 where M=Co, Cu, Zn and Mn) were performed on Vienna Ab-initio Simulation Package (VASP)[19] version 6.3.0. All calculations utilise a plane wave basis set for expansion of electron wavefunctions[20] and further use Projector Augmented Wave (PAW)[21] pseudopotentials for approximating the exchange-correlation functional, which for the systems under consideration are obtained from the Perdew−Burke−Ernzerhof (PBE) generalised gradient approximation (GGA) scheme.[22] The vacancy formation energy was calculated for each system using Equation 1.[1]

$$E_{VF} = (E_V + E_{M/Fe}) - E_o \qquad \text{Equation 1}$$

Here, E_{VF} represents the vacancy formation energy for the system; $E_o$represents the ground state energy of the defect-free supercells and, E_V refers to the ground state energy of the supercell with one random vacancy introduced by the removal of either a substituent (M) atom in the case of doped ferrite or a Fe atom in the case of undoped ferrite. $E_{M/Fe}$ is the energy of a single Fe/M atom that has been removed to create a vacancy in its most stable state and was calculated as the energy per atom of a defect-free unit cell of the particular element in its equilibrium crystal structure at 0 K (Fig. 1). All the aforementioned energies were obtained by performing self-consistent field (SCF) calculations while considering the ions in the supercell to be fixed in their experimentally reported lattice positions. Ionic relaxations were avoided to be able to accurately model only a single vacancy formation energy in an

[1] Freysoldt C, Grabowski B, Hickel T, Neugebauer J, Kresse G, Janotti A, Van de Walle CG. First-principles calculations for point defects in solids. Reviews of modern physics. 2014;86(1):253.

infinite lattice, for which the ionic cores must be essentially unperturbed.[2] More details related to the computational experimentation is added in Supporting Information

The defect-free hexagonal supercell considered for pure ferrite consisted of 42 atoms whereas the cubic supercells considered for all spinel ferrites were of size 56 atoms except in the case of copper ferrite which has a tetragonal unit cell of size 28 atoms. To standardise the vacancy formation energy calculations, the copper ferrite supercell was extended to double its length along its 'c' axis to remove any undesired size effects on the calculation of vacancy formation energy and to maintain uniform vacancy concentration across all spinel ferrite systems. Two different vacancy formation energies had to be calculated for all the systems either pertaining to the different element types (M and Fe vacancies for spinel ferrites) or the same element type being present in sites with different coordination numbers within the supercell (Fe in Fe_3O_4 in octahedral and tetrahedral sites).

The threshold energy for the plane wave basis set was chosen to be 450 eV which gives reasonably fast and accurate SCF calculations. Convergence criteria for electronic self-consistency was considered to be fulfilled when the difference between the total energy of the system in any two consecutive electronic steps was less than 10^{-8} eV. The k-point sampling over the Brillouin zone was performed using a centred k-points mesh for all systems. For all cubic systems, a k-point mesh of size 6x6x6 k-points was considered and for other geometries, the number of k-points along each axis was taken in proportion to the reciprocal of the length of that axis while typically limiting the maximum number of k-points along any axis to be less than or equal to 8.

Table S1: *Molar concentration of all the precursors used in synthesis of the ferrite nanoparticles*

[2] Van de Walle CG, Neugebauer J. First-principles calculations for defects and impurities: Applications to III-nitrides. Journal of applied physics. 2004;95(8):3851-79.

Comment []:
Editor's comment 2

Sample Sample	Molar concentration of $FeCl_3 \cdot 6H_2O$	Molar concentration of $FeCl_2 \cdot 4H_2O$	Molar concentration of dopant salt
Fe_3O_4	2 mM	1 mM	
$Cu_xFe_{3-x}O_4$	1.6 mM	0.8 mM	$CuCl_2 \cdot 2H_2O$ = 0.86 mM
$Co_xFe_{3-x}O_4$	1.6 mM	0.8 mM	$CoCl_2 \cdot 6H_2O$ = 1.1 mM
$Zn_xFe_{3-x}O_4$	1.6 mM	0.8 mM	$ZnCl_2 \cdot 2H_2O$ = 0.8 mM
$Mn_xFe_{3-x}O_4$	1.6 mM	0.8 mM	$MnCl_2 \cdot 4H_2O$ = 0.7 mM

Table S2: *Table showing the exposure of equivalent ionic concentration of ferrites in two scenarios (a) ferrites undergoing 100% dissolution, (b) actual/realistic dissolution as calculated from figure 3(a). These exposures were calculated as per the measurement values of ICP-MS.*

Sample	**Complete dissolution (µg mL^{-1})**	**Realistic/actual dissolution values (µg mL^{-1})**	
Fe_3O_4	Fe= 65.6	24 h	Fe= 3.19
		48 h	Fe= 3.33
		72 h	Fe= 3.61
$CuFe_2O_4$	Fe= 52.17 Cu= 15.8	24 h	Fe= 1.7; Cu= 1.2
		48 h	Fe= 1.6; Cu= 1
		72 h	Fe= 1.7; Cu= 1.37
$CoFe_2O_4$	Fe= 38 Co= 18.4	24 h	Fe= 5.9; Co= 2.4
		48 h	Fe= 4.9; Co= 3.6
		72 h	Fe= 5.9; Co= 3.3
$ZnFe_2O_4$	Fe= 36.6 Zn= 15.4	24 h	Fe= 1.5; Zn= 0.58
		48 h	Fe= 1.7; Zn= 0.63
		72 h	Fe= 2; Zn= 0.63
$MnFe_2O_4$	Fe= 32 Mn=16	24 h	Fe= 3.2; Mn= 2.0
		48 h	Fe= 5.6; Mn= 1.6
		72 h	Fe= 7.7; Mn= 2.2

Table S3: Table showing the inherent toxicity contribution of dopant secondary metal ions towards the overall observed toxicity.

Comment []:
Editor's Comment 8

Sample	*Time points*	*Total toxicity through dissolved ions (%)*	*Toxicity contribution by dopants ions (%)*
$CuFe_2O_4$	24 h	8.8	2.2
	48 h	26.9	12.3
	72 h	34.6	15.3
$CoFe_2O_4$	24 h	12.2	5.6
	48 h	24.1	9.6
	72 h	29.6	10.3
$ZnFe_2O_4$	24 h	9.2	2.7
	48 h	17.7	3.1
	72 h	27.6	8.31
$MnFe_2O_4$	24 h	15.5	8.9
	48 h	22.1	7.5
	72 h	29.6	10.3

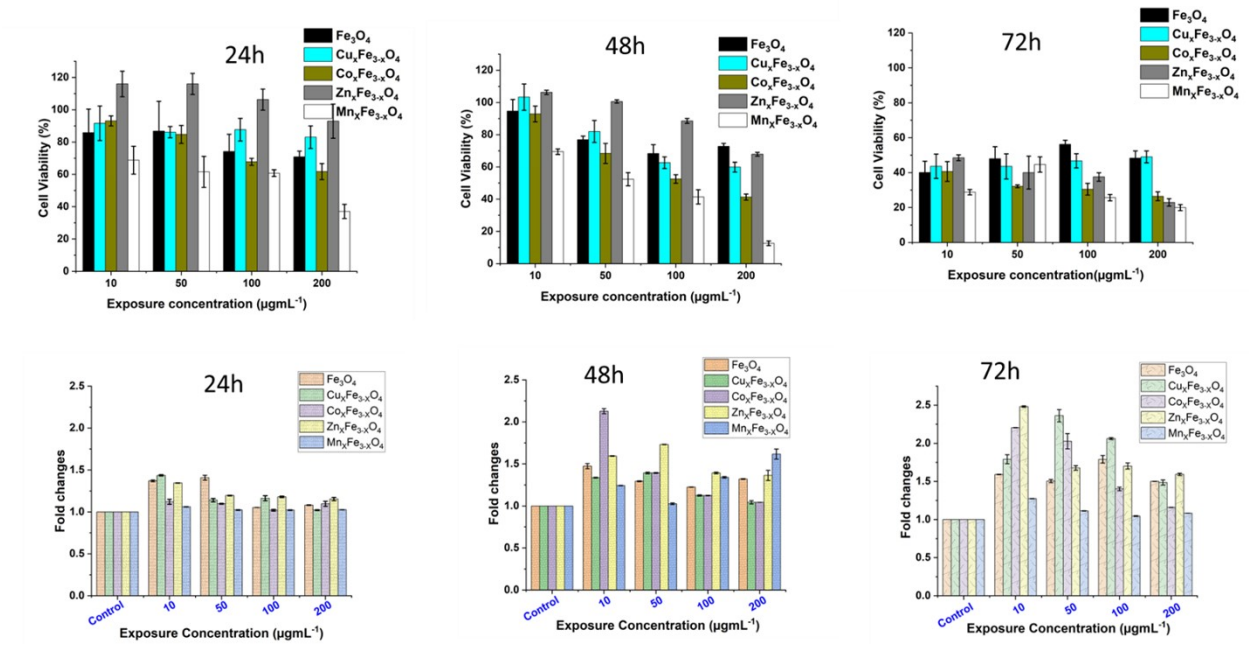

Figure S1: *Effect of doped ferrite nanoparticles on viability of A549 cells after (a) 24 h of exposure (b) 48 h of exposure (c) 72 h of exposure. Doped ferrite nanoparticle induced ROS generation after (d) 24 h of exposure (e) 48 h of exposure (f) 72 h of exposure. (n=3, data presented as mean± std.dev, calculated with respected to untreated control). The statistical analysis was performed with respect to control.*

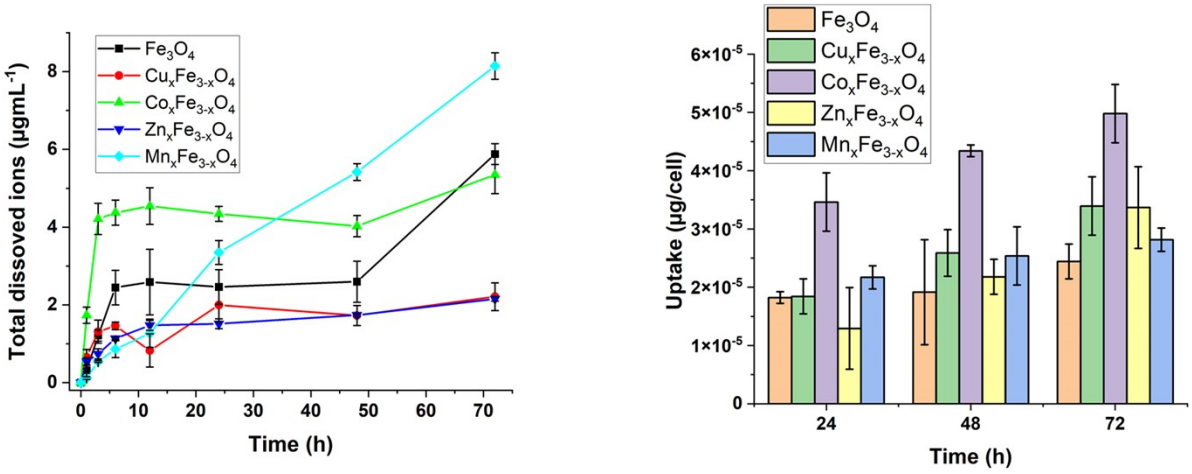

Figure S2: *(a) Profile of the dissolution (µg mL^{-1}) of ferrite nanoparticles with time. The concentration of each ferrite variant used for the experiments was 100 µg mL^{-1} upto 72 h in complete media (DMEM, 10% FBS). (b)Cell uptake measurements of the ferrite nanoparticles variants after 24 h, 48 h and 72 h of exposure to A549 cells. (n=3, data presented as mean±std.dev, uptake was calculated with respected to untreated control).*

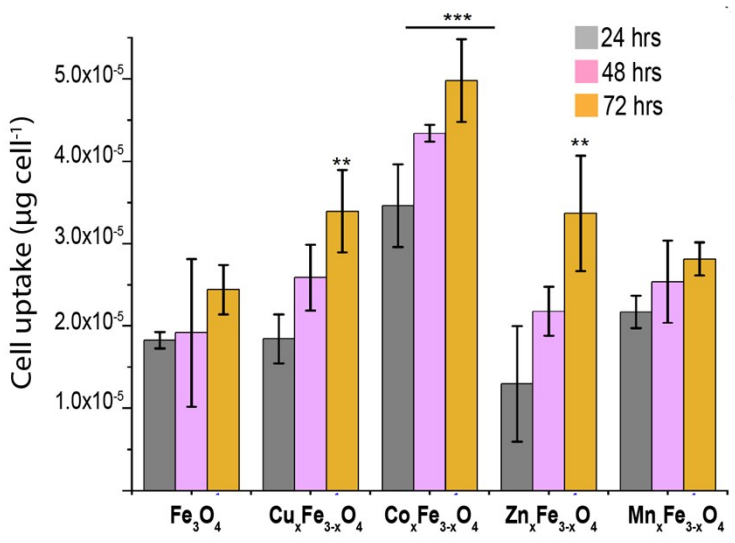

Figure S3: *Cell uptake measurements of the ferrite nanoparticles variants after 24h, 48h and 72h of exposure to A549 cells. (n=3, data presented as mean± std.dev., uptake was calculated with respected to untreated control).*

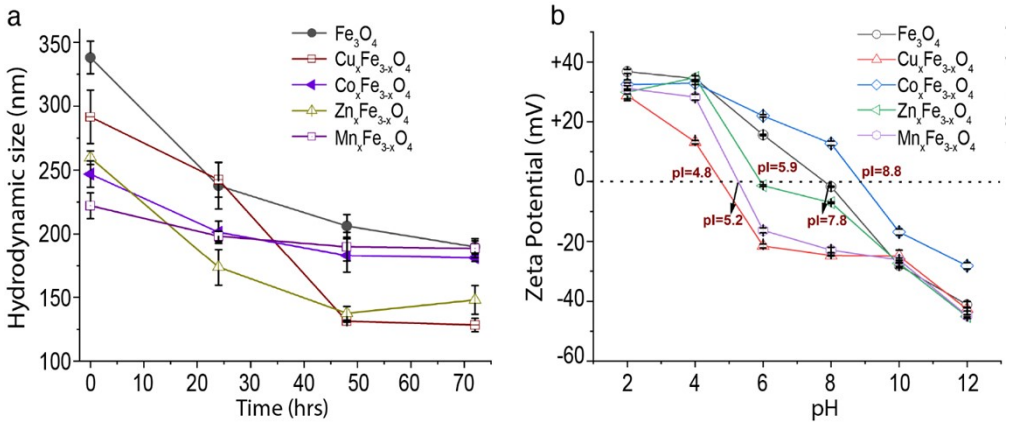

***Figure S4**: Nanoparticle suspension stability analysis by hydrodynamic size and zeta potential (a) Hydrodynamic stability profile of all ferrite nanoparticles at a concentration of 100 µg mL^{-1}at 37°C in complete media (DMEM, 1% FBS) for 72h (b) pH vs. Zeta potential measurements of the ferrite nanoparticles 100 µg mL^{-1} at 37°C at various pH (2-12). The experiments were performed in triplicate (n=3).*

Comment []:
Editorial correction

Comment []:
Editorial correction

Comment []:
Editorial correction

References used in (Figure 8)

Figure 8(a)

1. Cronholm P, et al. Intracellular uptake and toxicity of Ag and CuO nanoparticles: a comparison between nanoparticles and their corresponding metal ions. Small. 2013;9(7):970-82.

2. Preethi DR, et al. Anticancer activity of pure and silver doped copper oxide nanoparticles against A549 Cell line. Materials Today Communications. 2022;33:104462

3. Wu R, et al. Spatio-design of multidimensional prickly Zn-doped CuO nanoparticle for efficient bacterial killing. Advanced Materials Interfaces. 2016;3(18):1600472.

4. Elemike EE, et al. CuO and Au-CuO nanoparticles mediated by Stigmaphyllon ovatum leaf extract and their anticancer potential. Inorganic Chemistry Communications. 2019;104:93-7.

5. Jan T, et al. Structural, Raman and optical characteristics of Sn doped CuO nanostructures: a novel anticancer agent. Ceramics International. 2015;41(10):13074-9.

6. Naatz H, et al. Safe-by-design CuO nanoparticles via Fe-doping, Cu–O bond length variation, and biological assessment in cells and zebrafish embryos. ACS nano. 2017;11(1):501-15.

Figure 8(b)

1. Hamidian K, et al. Cytotoxicity evaluation of green synthesized ZnO and Ag-doped ZnO nanoparticles on brain glioblastoma cells. Journal of Molecular Structure. 2022;1251:131962.

2. Hamidian K, et al. Cytotoxic performance of green synthesized Ag and Mg dual doped ZnO NPs using Salvadora persica extract against MDA-MB-231 and MCF-10 cells. Arabian Journal of Chemistry. 2022;15(5):103792.

3. Shakir M, et al. Photocatalytic degradation of the Paracetamol drug using Lanthanum doped ZnO nanoparticles and their in-vitro cytotoxicity assay. Journal of Luminescence. 2016;176:159-67.

4. Thurber A, et al. Improving the selective cancer killing ability of ZnO nanoparticles using Fe doping. Nanotoxicology. 2012;6(4):440-52.

Figure 8(c)

1. Manikandan K, et al. Facile synthesis and characterization of W-doped TiO2 nanoparticles: Promising ancticancer activity with high selectivity. Inorganic Chemistry Communications. 2021;132:108855.

2. Barkhade T, et al. Effect of TiO2 and Fe doped TiO2 nanoparticles on mitochondrial membrane potential in HBL-100 cells. Biointerphases. 2019;14(4):041003.

3. Nakayama M, et al. Samarium doped titanium dioxide nanoparticles as theranostic agents in radiation therapy. Physica Medica. 2020;75:69-76.

4. Ahamed M, et al. Ag-doping regulates the cytotoxicity of TiO2 nanoparticles via oxidative stress in human cancer cells. Scientific reports. 2017;7(1):17662.

5. Zahid M, et al. Fabrication of visible light-induced antibacterial and self-cleaning cotton fabrics using manganese doped TiO2 nanoparticles. ACS Applied Bio Materials. 2018;1(4):1154-64.

6. Yang CC, et al. Development of Ce-doped TiO2 activated by X-ray irradiation for alternative cancer treatment. Ceramics International. 2017;43(15):12675-83.

7. Ahmad J, et al. Copper doping enhanced the oxidative stress–mediated cytotoxicity of TiO2 nanoparticles in A549 cells. Human & experimental toxicology. 2018;37(5):496-507.

Figure 8(d)

1. Maleki P, et al. Green facile synthesis of silver-doped cerium oxide nanoparticles and investigation of their cytotoxicity and antibacterial activity. Inorg. Chem. Comm. 2021;131:108762.

2. Atif M, et al. Manganese-doped cerium oxide nanocomposite induced photodynamic therapy in MCF-7 cancer cells and antibacterial activity. BioMed Research International. 2019;2019.

3. Hamidian K, et al. Doped and un-doped cerium oxide nanoparticles: Biosynthesis, characterization, and cytotoxic study. Ceramics Int. 2021;47(10):13895-902.

4. Akbari A, et al. Zinc-doped cerium oxide nanoparticles: Sol-gel synthesis, characterization, and investigation of their in vitro cytotoxicity effects. J. Mol. Structure. 2017;1149:771-6.

5. Abbas F, et al. Facile synthesis of ferromagnetic Ni doped CeO2 nanoparticles with enhanced anticancer activity. App. Surf. Sci. 2015;357:931-6.